

# TOI-1442 b and TOI-2445 b: two ultra-short period super-Earths around M dwarfs

G. Morello<sup>1,2,3</sup>, H. Parviainen<sup>1,2</sup>, F. Murgas<sup>1,2</sup>, E. Pallé<sup>1,2</sup>, M. Oshagh<sup>1,2</sup>, A. Fukui<sup>5,1</sup>, T. Hirano<sup>6,13</sup>, H. T. Ishikawa<sup>6,13</sup>, N. Narita<sup>5,6,1</sup>, K. A. Collins<sup>7</sup>, K. Barkaoui<sup>26,27,1</sup>, P. Lewin<sup>8</sup>, C. Cadieux<sup>9</sup>, J. P. de Leon<sup>14</sup>, A. Soubkiou<sup>29</sup>, N. Crouzet<sup>11</sup>, E. Esparza-Borges<sup>1,2</sup>, Y. Hori<sup>6,13</sup>, M. Ikoma<sup>24</sup>, K. Isogai<sup>15,16</sup>, T. Kagitani<sup>16</sup>, K. Kawauchi<sup>1,2</sup>, T. Kimura<sup>23</sup>, T. Kodama<sup>5</sup>, J. Korth<sup>18,19</sup>, T. Kotani<sup>6,13,17</sup>, V. Krishnamurthy<sup>6,13</sup>, S. Kurita<sup>23</sup>, J. H. Livingston<sup>14</sup>, R. Luque<sup>20</sup>, A. Madrigal-Aguado<sup>1,2</sup>, M. Mori<sup>14</sup>, T. Nishiumi<sup>17,6,16</sup>, J. Orell-Miquel<sup>1,2</sup>, M. Tamura<sup>14,6,13</sup>, Y. Terada<sup>21,22</sup>, N. Watanabe<sup>16</sup>, Y. Zou<sup>16</sup>, Z. Benkhaldoun<sup>29</sup>, K. I. Collins<sup>30</sup>, R. Doyon<sup>10</sup>, L. Garcia<sup>26</sup>, M. Ghachoui<sup>26,29</sup>, M. Gillon<sup>26</sup>, E. Jehin<sup>28</sup>, E. L. N. Jensen<sup>31</sup>, D. W. Latham<sup>7</sup>, F. J. Pozuelos<sup>26,28</sup>, R. P. Schwarz<sup>32</sup>, and M. Timmermans<sup>26</sup>

(Affiliations can be found after the references)

February 1, 2022

## ABSTRACT

**Context.** Exoplanets with orbital periods of less than one day are known as Ultra-short period (USP) planets. They are relatively rare products of planetary formation and evolution processes, but especially favourable to current planet detection methods. At the time of writing, 120 USP planets have already been confirmed.

**Aims.** We aim to confirm the planetary nature of two new transiting planet candidates announced by the NASA's Transiting Exoplanet Survey Satellite (TESS), registered as TESS Objects of Interest (TOIs) TOI-1442.01 and TOI-2445.01.

**Methods.** We use the TESS data, ground-based photometric light-curves and Subaru/IRD spectrograph radial velocity (RV) measurements to validate both planetary candidates and to establish their physical properties.

**Results.** TOI-1442 b is a hot super-Earth with an orbital period of  $P = 0.4090682 \pm 0.0000004$  d, a radius of  $R_p = 1.27^{+0.50}_{-0.44} R_\oplus$ , equilibrium temperature of  $T_{p,eq} = 1359^{+49}_{-42}$  K, and a mass  $M_p < 18 M_\oplus$  at  $3\sigma$ . TOI-2445 b is also a hot super-Earth/mini-Neptune with an orbital period of  $P = 0.3711286 \pm 0.0000004$  d, a radius of  $R_p = 1.52^{+1.20}_{-0.26} R_\oplus$ , equilibrium temperature of  $T_{p,eq} = 1332^{+61}_{-57}$  K, and a mass  $M_p < 38 M_\oplus$  at  $3\sigma$ . Their physical properties align with current empirical trends and formation theories of USP planets. More RV measurements will be useful to constrain the planetary masses and mean densities, as well as the predicted presence of outer planetary companions.

**Key words.** planetary systems – planets and satellites: individual: TOI-1442 b, TOI-2445 b – techniques: photometric – techniques: spectroscopic – methods: observational

## 1. Introduction

The main theories of planetary formation based on our Solar System did not predict the existence of planets on orbits much narrower than that of Mercury. However, since the discovery of the first hot Jupiter (Mayor & Queloz 1995), many exoplanets have been detected with orbital periods of just a few days. Among the close-in planet population, the ultra-short period (USP) planets are defined as the ones that complete their entire orbit in less than one day (Sahu et al. 2006). These extreme cases may provide some of the most revealing insights into the formation and evolution processes of planetary systems. They are also excellent test beds for studying star-planet interactions, such as the effects of tidal forces and atmospheric erosion processes.

All other conditions being equal, USP planets are the easiest to detect and characterise by means of occultations and radial velocity measurements (Gaudi et al. 2005). Despite this strong selection bias, the observed period distribution of exoplanets drops at  $P \lesssim 4$  d (see Figure 1), indicating that planets with shorter orbital periods are increasingly rare. Recent estimates of the occurrence rate of USP planets are  $\sim 0.5\%$  (Sanchis-Ojeda et al. 2014; Winn et al. 2018; Zhu & Dong 2021; Uzsoy et al. 2021), which is comparable with the frequency of hot Jupiters (Howard et al. 2012; Fressin et al. 2013; Wang et al. 2015; Zhu & Dong 2021). Additionally, more than 80% of the known USP popu-

lation have radii  $R_p < 2 R_\oplus$ . There are only eight USP Jupiters with  $0.75 < P < 1$  d. Both the frequency and the small size of USP planets have suggested that they could be the remnant rocky cores of evaporated hot Jupiters (Valsecchi et al. 2014; Königl et al. 2017). The lack of a metallicity trend for the USP planet host stars, unlike hot Jupiters, limits the maximum relative frequency for this evolutionary path (Fischer & Valenti 2005; Winn et al. 2017). Other proposed pathways include photoevaporation of gaseous sub-Neptunes (Lundkvist et al. 2016; Lee & Chiang 2017), in situ formation (Chiang & Laughlin 2013), and inward migration of rocky planets (Petrovich et al. 2019). The latter hypothesis finds empirical support as several USP planets are part of compact systems showing a broad range of mutual inclinations (Petrovich et al. 2020).

In this paper, we report the discovery of two USP super-Earths around M dwarfs from the Transiting Exoplanet Survey Satellite (TESS) and ground-based follow-up programs. This paper is structured as follows. Section 2 describes the observations. In particular, Section 2.1 describes the TESS observations, Section 2.2 the ground-based transit photometry, and Section 2.3 the spectroscopic observations. Section 3 discusses the characterisation of the host stars. Sections 4 and 5 explain the methods to analyse the transit photometric observations and spectroscopic radial velocities. Section 6 reports the results of our analyses.

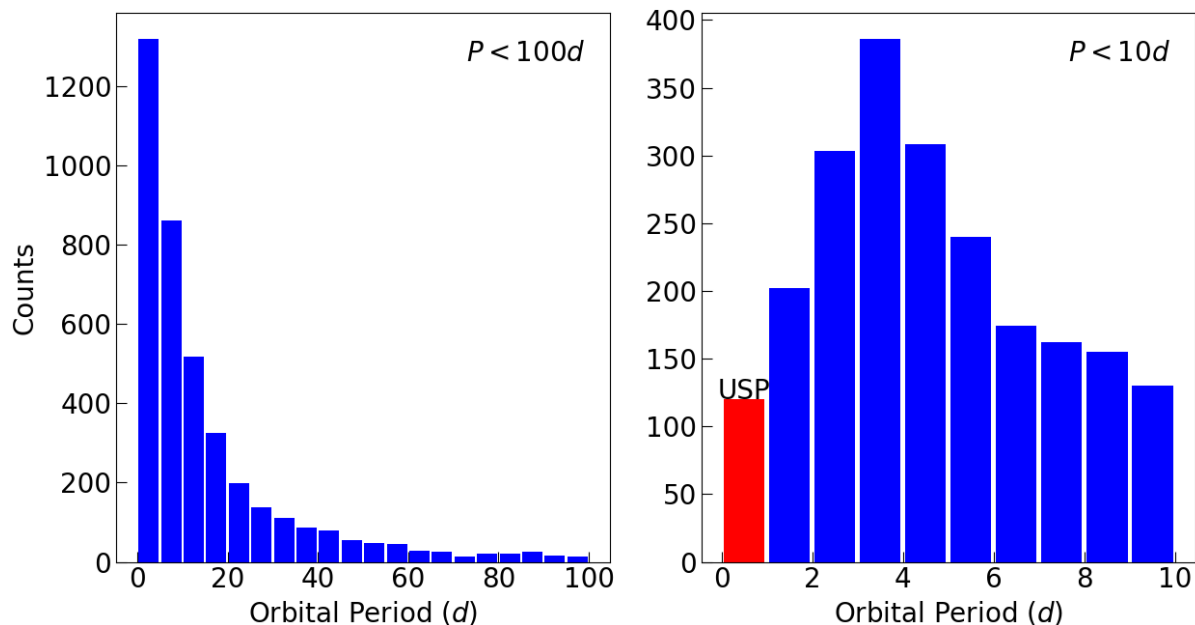


**Fig. 1.** Left panel: Orbital period distribution of the confirmed exoplanets with  $P < 100 d$ , based on NASA Exoplanet Archive data as of 2022 January 28. Right panel: Period distribution of the subset of exoplanets with  $P < 10 d$ ; the red bar denotes the number of USP planets. Note that selection effects favour the discovery of planets with shorter orbital periods, so that the observed distributions are not necessarily representative of the underlying population. However, the decrease in frequency at  $P < 4 d$  must be real, as such planets are easier to detect than those with longer periods.

Section 7 put them into the scientific context. Section 8 summarizes our findings.

## 2. Observations

### 2.1. TESS photometry

TOI-1442 (TIC 235683377) was observed by TESS in 2 min short-cadence integrations during sectors 14 to 26 (2019 July 18 - 2020 July 04) and 40 to 41 (2021 June 25 - 2021 August 20). It was announced on 2019 November 14 as a TESS object of interest (TOI) by the Science Processing Operations Center (SPOC) pipeline at NASA Ames Research Center.

TOI-2445 (TIC 439867639) was observed by TESS in 2 min short-cadence integrations during sectors 4 (2018 October 19 - 2018 November 14) and 31 (2020 October 22 - 2020 November 16). It was announced on 2021 January 6 as a TOI detected also by SPOC.

We downloaded the data from the Mikulski Archive for Space Telescopes<sup>1</sup> (MAST) and extracted the Pre-search Data Conditioned Simple Aperture Photometry (PDCSAP) from the light-curve files (extension: ‘\_lc.fits’). The PDCSAP timeseries were computed by the SPOC pipeline (Jenkins et al. 2016), that calibrates the image data, performs quality control (e.g., flags bad data), calculates the flux for each target in the field of view through simple aperture photometry (SAP module, Morris et al. 2020), and corrects for instrumental systematic effects (PDC module, Smith et al. 2012; Stumpe et al. 2014). Figure 2 shows the target pixel files (TPFs) and aperture masks used to extract the SAP flux, created using *tpfplotter*<sup>2</sup> (Aller et al. 2020). There are no known contaminants falling within the aperture

masks in most sectors, except for a fainter source with  $\Delta m > 3$  with respect to TOI-1442 in sectors 15, 18, 21, 26 and 41.

### 2.2. Ground-based photometry

The TESS Follow-up Observing Program (TFOP) is a network of observatories and researchers aiming to validate the planetary nature of transit-like signals tagged as TOIs, to measure the masses and radii of the planets, as well as the orbital properties and the stellar host parameters. We make use of transit photometry data acquired under the TFOP to confirm that the planetary transits occur on the targeted stars, rule out some false positive scenarios (e.g., blended eclipsing binaries), and refine the planet’s radius measurement. The TFOP data are available to the working group members on the Exoplanet Follow-up Observing Program for TESS (ExoFOP-TESS)<sup>3</sup> website.

#### 2.2.1. MuSCAT

The Multi-colour Simultaneous Camera for studying Atmospheres of Transiting planets (MuSCAT, Narita et al. 2015) is a three-band imager mounted on the 188-cm telescope of National Astronomical Observatory of Japan in Okayama, Japan. MuSCAT is equipped with three 1024×1024 pixel CCDs with pixel scale of  $0''.358 \text{ pixel}^{-1}$ . The field of view of MuSCAT is  $6'.1 \times 6'.1$ . Each CCD is coupled with an Astrodon Photometrics Generation 2 Sloan filter. The three filter bands are  $g$  (400-550 nm),  $r$  (550-700 nm) and  $z_s$  (820-920 nm).

We observed a full transit of TOI-2445 b on 2021 February 7 UT with MuSCAT. The exposure times were 30, 20 and 35 s for the  $g$ ,  $r$  and  $z_s$  bands, respectively. After performing dark and flatfield calibrations, we extracted light-curves by aperture pho-

<sup>1</sup> <https://mast.stsci.edu>

<sup>2</sup> <https://github.com/jlillo/tpfplotter>

<sup>3</sup> <https://exofop.ipac.caltech.edu/tess/>

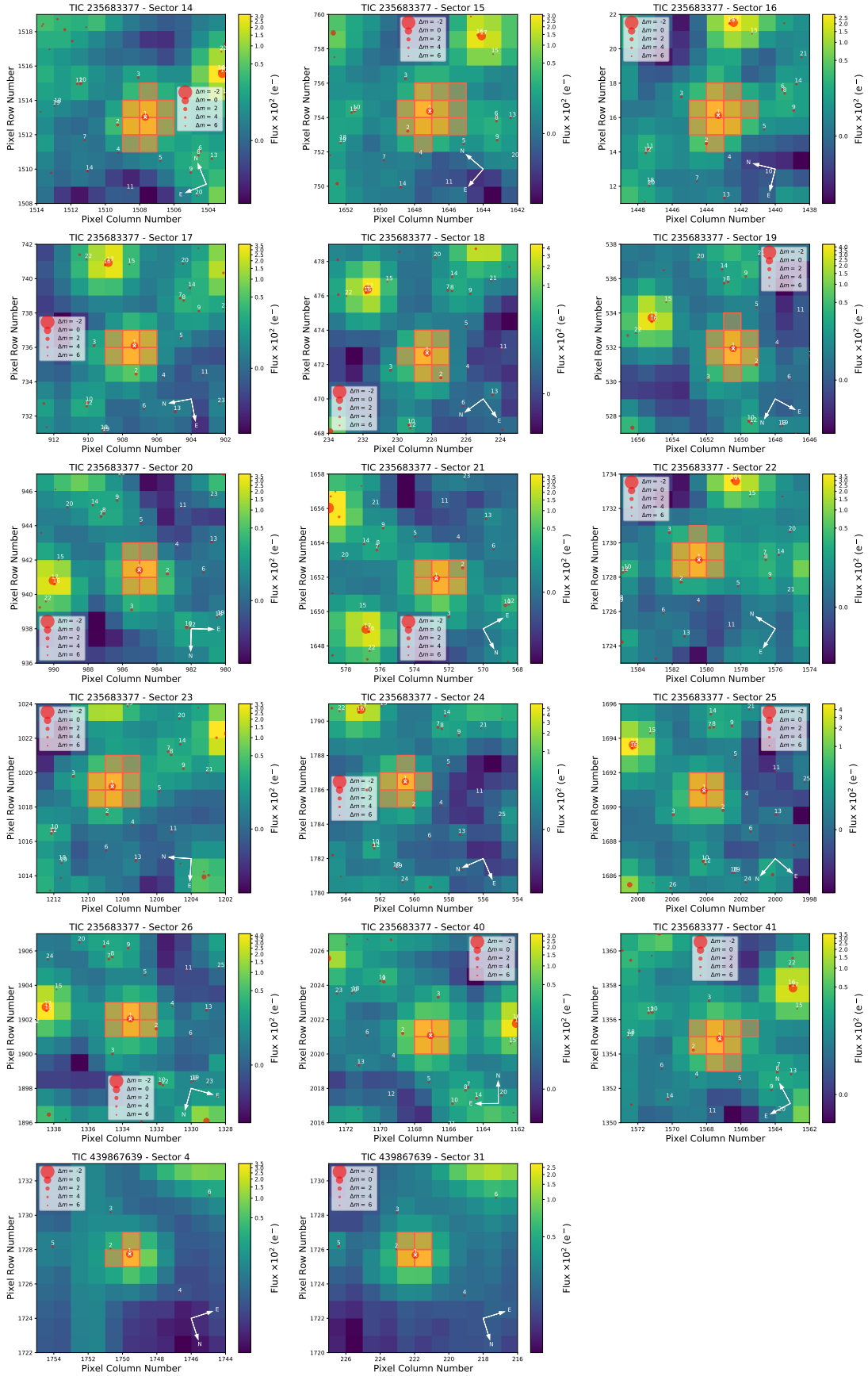


**Fig. 2.** TESS target pixel file images of TOI-1442 (top 15 panels) and TOI-2445 (last two panels). The pixels highlighted in red denote the aperture mask used to calculate the SAP. The red circles represent neighboring sources listed in Gaia DR2, the target star being marked with a white "x" and identifier 1. The size of the red circles is inversely proportional to the apparent magnitude difference with respect to the target star.

tometry with radii of  $3''.6$ ,  $4''.3$ , and  $3''.6$  using a custom data reduction pipeline (Fukui et al. 2011). The resulting photometric dispersion per exposure are 1.4%, 0.7% and 0.2%.

### 2.2.2. MuSCAT2

MuSCAT2 (Narita et al. 2019) is a four-band imager mounted on the 152-cm Telescopio Carlo Sánchez (TCS) at Teide Observatory in Spain. MuSCAT2 is equipped with four  $1024 \times 1024$  pixel CCDs with pixel scale of  $0''.435 \text{ pixel}^{-1}$ . The field of view of MuSCAT2 is  $7'.4 \times 7'.4$ . The four filter bands are  $g$  (400–550 nm),  $r$  (550–700 nm),  $i$  (700–820 nm) and  $z_s$  (820–920 nm). Three  $g$ ,  $r$  and  $z_s$  filters are identical to those adopted by MuSCAT. The  $i$  filter was custom-ordered and manufactured by Asahi Spectra Co., Ltd.

We observed a partial transit of TOI-2445 b on 2021 August 6 UT, and a full transit on 2021 September 14 UT with MuSCAT2. The  $r$  filter was not available during the last observation. The exposure times were set between 50 and 100 s, depending on the band, instrument and observing conditions. We extracted photometry with aperture radii of  $10''.875$ . The resulting photometric dispersion per exposure are 0.53–0.42% in  $g$ , 0.29% in  $r$ , 0.33–0.25% in  $i$ , and 0.24–0.27% in  $z_s$  for the two nights, respectively.

### 2.2.3. MuSCAT3

MuSCAT3 (Narita et al. 2020) is another four-band imager with  $g$ ,  $r$ ,  $i$  and  $z_s$  filters, mounted on the 2-m Faulkes Telescope North (FTN) of Las Cumbres Observatory at the Haleakala observatory in Hawaii. The  $2048 \times 2048$  pixel CCDs, with pixel scale of  $0''.266 \text{ pixel}^{-1}$ , were manufactured by Teledyne Princeton Instruments. The field of view of MuSCAT3 is  $9'.1 \times 9'.1$ .

We observed three transits of TOI-1442 b on 2021 May 05, 2021 June 06 and 2021 June 17 UT with MuSCAT3. We discarded the  $g$  band data from the first two observations, because of too high scatter. The exposure times were set to 240, 67, 30 and 29 s for the  $g$ ,  $r$ ,  $i$  and  $z_s$  bands, respectively. We extracted photometry with aperture radii of  $2''.65$ ,  $7''.95$  and  $4''.68$ . The resulting photometric dispersion per exposure are 0.078% in  $g$ , 0.054–0.064% in  $r$ , 0.62–0.94% in  $i$ , and 0.39–0.68% in  $z_s$ .

### 2.2.4. TRAPPIST-South

The TRAnsiting Planets and Planetesimals Small Telescope–South (TRAPPIST-South, Jehin et al. 2011; Gillon et al. 2011) is a 60-cm telescope at La Silla Observatory in Chile. It is equipped with a thermoelectrically cooled  $2K \times 2K$  pixel FLI Proline PL3041-BB CCD with pixel scale of  $0''.64 \text{ pixel}^{-1}$ , resulting a field of view of  $22' \times 22'$ .

We observed two transits of TOI-2445 b on 2021 January 8 and 14 in the  $I+z$  filter with an exposure time of 50 s. We used the TESS Transit Finder tool, which is a customized version of the Tapir software package (Jensen 2013), to schedule the photometric time-series. Data calibration and photometric measurements were performed using the *PROSE*<sup>4</sup> pipeline (Garcia et al. 2021).

### 2.2.5. LCOGT 1 m

We observed four full transits of TOI-1442 b from the Las Cumbres Observatory Global Telescope (LCOGT; Brown et al. 2013)

<sup>4</sup> <https://github.com/lgrcia/prose>

1.0 m network node at McDonald Observatory. Observations on 2020 August 14 and 2020 August 30 were conducted in I-band, and observations on 2020 September 26 and 2020 October 21 were conducted in Sloan  $i'$  band. We used the TESS Transit Finder to schedule our transit observations. The 1 m telescopes are equipped with  $4096 \times 4096$  pixel SINISTRO cameras having an image scale of  $0''.389$  per pixel, resulting in a  $26' \times 26'$  field of view. The images were calibrated by the standard LCOGT BANZAI pipeline (McCully et al. 2018), and photometric data were extracted using *AstroImageJ* (Collins et al. 2017). The images were focused and have mean stellar point-spread-functions with a FWHM of  $\sim 2''$ , and circular photometric apertures with radius  $\sim 4''$  were used to extract the differential photometry. The apertures exclude flux from the nearest Gaia EDR3 and TESS Input Catalog neighbor (TIC 1718221659)  $13''$  west of the target.

### 2.2.6. OMM/PESTO

We observed a full transit of TOI-1442 b at Observatoire du Mont-Mégantic, Canada, on 2020 February 9. The observations were made in the  $i'$  filter using the 1.6 m telescope of the observatory equipped with the PESTO camera. The light curve extraction via differential photometry was accomplished with *AstroImageJ*, which was also used for image calibration (bias subtraction and flat field division). The images have typical stellar point-spread-functions with a FWHM of  $\sim 2''$ , and circular photometric apertures with radius  $\sim 5''$  were used to extract the differential photometry, excluding flux from the nearest Gaia EDR3 neighbour.

### 2.2.7. MLO/Lewin

We observed a full transit of TOI-2445 b in I-band on 2021 January 10 from the Maury Lewin Astronomical Observatory 0.36 m telescope near Glendora, CA. The telescope is equipped with  $3326 \times 2504$  pixel SBIG STF8300M camera having an image scale of  $0''.84$  per pixel, resulting in a  $23' \times 17'$  field of view. The images were calibrated and the photometric data were extracted using *AstroImageJ*. The images have typical stellar point-spread-functions with a FWHM of  $\sim 5''$ , and circular photometric apertures with radius  $\sim 7''$  were used to extract the differential photometry, which excluded most of the flux from the nearest Gaia EDR3 neighbour.

## 2.3. Spectroscopic observations with Subaru/IRD

The InfraRed Doppler (IRD) instrument on the 8.2m Subaru telescope is a fiber-fed spectrograph covering the wavelength range 930–1740 nm with a spectral resolution of  $R \sim 70\,000$  (Tamura et al. 2012; Kotani et al. 2018). We obtained 20 IRD spectra of TOI-1442 on 11 nights between 2020 September 27 and 2021 October 22 UT. We also obtained 12 IRD spectra of TOI-2445 on 5 nights between 2021 September 9 and 2021 November 12 UT. The exposure times were set to 1200–1800 s for TOI-1442 and 900–1800 s for TOI-2445, depending on the observing conditions. For all scientific exposures, we also injected the laser-frequency comb into the spectrograph, whose spectra were used for the simultaneous wavelength calibrations.

We reduced raw IRD data and extracted one-dimensional stellar and reference (laser-frequency comb) spectra as described in Hirano et al. (2020). Wavelengths were calibrated by using the data of the Thorium-Argon hollow-cathode lamp as well as

the laser-frequency comb taken during the daytime. Using IRD’s standard analysis pipeline (Hirano et al. 2020), we measured precise radial velocities (RVs) for both TOI-1442 and TOI-2445. In short, we extracted a template spectrum for each target that is free from telluric features and instrumental broadening based on multiple observed frames, and relative RVs were measured with respect to this template by the forward modeling technique taking into account the instantaneous instrumental profile of the spectrograph and telluric absorptions. The resulting RV precisions (internal errors) were typically  $4 - 5 \text{ m s}^{-1}$  for TOI-1442 and  $5 - 8 \text{ m s}^{-1}$  for TOI-2445, respectively.

### 3. Stellar characterisation

We applied the following procedure to determine the main stellar parameters relevant to the light-curve analysis: First, we derived the effective temperature ( $T_{*,\text{eff}}$ ), iron abundance ( $[Fe/H]_*$ ), and overall metallicity ( $[M/H]_*$ ) from the telluric-free template IRD spectra by following the same analysis as in Ishikawa et al. (2022). The template spectra were extracted for the purpose of radial velocity measurement described in Section 5. Note that for TOI-2445, we dared to use the spectrum without instrumental-profile deconvolution. This is because the SNR per frame of TOI-2445 is so low that the noise is amplified during the deconvolution, especially in the Y-band.

We used the 47 FeH molecular lines in the Wing-Ford band at 990 – 1020 nm to estimate  $T_{*,\text{eff}}$ . Note that the errors given in Tables 1 and 2 do not include any possible systematic errors but only the standard deviation ( $\sigma$ ) of estimates based on individual FeH lines divided by the square root of the number of lines ( $\sigma/\sqrt{N}$ ). More details can be found in Ishikawa et al. (2022). For elemental abundances, we used 34 and 30 neutral atomic lines for TOI-1442 and TOI-2445, respectively. The atomic species responsible for these lines are Na, Mg, Ca, Ti, Cr, Mn, Fe, and Sr. The analyses are based on the equivalent width comparison of individual absorption lines between the calculated model spectra and the observed ones. The detailed procedures to determine individual elemental abundances and their errors are also described in Ishikawa et al. (2020).

We alternated between  $T_{*,\text{eff}}$  estimation and abundance analysis to obtain  $T_{*,\text{eff}}$  and metallicity that are consistent with each other. Firstly, we derived a provisional  $T_{*,\text{eff}}$  adopting the solar metallicity ( $[Fe/H]_* = 0$ ), and then, we determined the individual abundances of the eight elements  $[X/H]_*$  using the  $T_{*,\text{eff}}$ . Secondly, we redetermined  $T_{*,\text{eff}}$  adopting the iron abundance  $[Fe/H]_*$  as the input metallicity, and then, we redetermined the abundances using the new  $T_{*,\text{eff}}$ . We iterated the estimation of  $T_{*,\text{eff}}$  and  $[Fe/H]_*$  until the final results and the results of the previous step agreed within the error margin. From the final results the abundances of the eight elements,  $[M/H]_*$  was determined by calculating the average weighted by the inverse of the square of their estimated errors.

Second, we performed SED fitting on the photometric magnitudes of Gaia EDR3 (Gaia Collaboration et al. 2021), 2MASS (Skrutskie et al. 2006), and WISE (Cutri et al. 2021), applying the  $[M/H]_*$  prior from the spectral analysis. Hence, we obtained an independent estimate of  $T_{*,\text{eff}}$ , along with the stellar radius ( $R_*$ ) and luminosity ( $L_*$ ). Specifically, the SED was calculated from the magnitudes in the Gaia EDR3  $G$ ,  $BP$ , and  $RP$  bands, 2MASS  $J$ ,  $H$ , and  $K_s$  bands, and WISE  $W1$ ,  $W2$ , and  $W3$  bands. The BT-Settl synthetic spectra (Allard 2014) were then fitted to the SED with the parameters of  $T_{*,\text{eff}}$ ,  $[M/H]_*$ , log surface gravity ( $\log g_*$ ), and  $\log(R_*/D)$ , where  $D$  is the distance to the system.

We calculated the posterior probability distributions of these parameters using the Markov Chain Monte Carlo (MCMC) method implemented in the Python package emcee (Foreman-Mackey et al. 2013). In each MCMC step, a synthetic spectrum was calculated by linearly interpolating the model grid for a given set of parameters. A Gaussian prior from IRD was applied for  $[M/H]_*$ . A white noise jitter term,  $\sigma_{\text{jitter}}$ , was also fitted for each of the Gaia EDR3, 2MASS and WISE data sets such that the magnitude uncertainty was given by  $\sqrt{\sigma_{\text{cat}}^2 + \sigma_{\text{jitter}}^2}$ , where  $\sigma_{\text{cat}}$  is the catalogued uncertainty in magnitude. Using the obtained posteriors of  $\log(R_*/D)$  and  $T_{*,\text{eff}}$ , we also derived the posteriors of  $R_*$  and  $L_*$  applying the distance from Bailer-Jones et al. (2021) for  $D$ .

Finally, we estimated the stellar mass ( $M_*$ ) and radius from  $[Fe/H]_*$  and the absolute  $K_s$  magnitude via the empirical relations of Mann et al. (2019) and Mann et al. (2015), respectively.

Tables 1 and 2 report the stellar parameters obtained with the three methods and values adopted from the literature. The parameter values obtained with multiple methods are consistent within  $1\sigma$ . The  $\log g_*$  is weakly constrained by SED fitting. The empirical relations provide the most precise determinations of  $M_*$ ,  $\rho_*$  and  $\log g_*$ .

### 4. Light-curve analysis

#### 4.1. Contamination transit models

In order to confirm the planetary nature of our TOIs, we fitted simultaneously the TESS and ground-based photometric light-curves by modeling planetary transits with third light contamination. Our approach is similar to that described by Parviainen et al. (2019, 2020, 2021).

The transit models were generated with a customised version of PYLIGHTCURVE<sup>5</sup> (Tsiaras et al. 2016), which implements the analytic formulae derived by Pál (2008). Conventionally, the model light-curves are normalised so that the out-of-transit flux is unity, and the flux drop during transit corresponds to the fraction of stellar flux occulted by the transiting planet. We fitted the following transit parameters: planet-to-star radius ratio ( $p = R_p/R_*$ ), orbital period ( $P$ ), epoch of transit ( $T_0$ ), total transit duration ( $T_{14}$ ), stellar mean density ( $\rho_*$ ), and two limb-darkening coefficients (LDCs,  $q_1$  and  $q_2$ ). We assumed the power-2 law to approximate the stellar limb-darkening profile (Hestroffer 1997), as recommended by Morello et al. (2017), especially for M dwarfs. Additionally, we implemented optimal sampling by means of the transformed LDCs,  $q_1$  and  $q_2$ , derived by Short et al. (2019) following the procedure of Kipping (2013).

Third light generally means any contribution to the flux from sources outside the star-planet system, such as blended or nearby stars of which part of the photons hit the selected photometric aperture of the target. In this work, we define the relative third light flux as

$$\beta = \frac{F_c}{F_* + F_c}, \quad (1)$$

where  $F_*$  and  $F_c$  denote the flux from the target star and contaminating sources, respectively. Thus, the contaminated transit model can be expressed as

$$\hat{F}(t) = (1 - \beta)(1 - \Lambda(t)) + \beta, \quad (2)$$

where  $\hat{F}(t)$  is the normalised astrophysical flux, and  $1 - \Lambda(t)$  is the pure planetary transit model. We further assumed that

<sup>5</sup> <https://github.com/ucl-exoplanets/pylightcurve>

**Table 1.** Stellar properties of TOI-1442.

Parameter	Value			Reference <sup>a</sup>
Astrometric Parameters				
$\alpha$ (epoch 2016.0)	19:9:10.1142			(1)
$\delta$ (epoch 2016.0)	+74:10:27.626			(1)
$\mu_\alpha$ (mas/yr)	81.959 $\pm$ 0.020			(1)
$\mu_\delta$ (mas/yr)	462.708 $\pm$ 0.017			(1)
Parallax (mas)	24.164 $\pm$ 0.015			(1)
Distance (pc)	41.316 $\pm$ 0.023			(2)
Photospheric Parameters				
	Spec. Synth.	SED fit	Emp. Rel.	
$T_{*,\text{eff}}$ (K) <sup>b</sup>	3345 $\pm$ 13	3263 <sup>+33</sup> <sub>-22</sub>		This work
$\log g_*$ (dex)		5.27 <sup>+0.17</sup> <sub>-0.37</sub>	4.91 $\pm$ 0.03	This work
$[M/H]_*$ (dex)	0.10 $\pm$ 0.07	0.12 $\pm$ 0.07		This work
$[Fe/H]_*$ (dex)	0.03 $\pm$ 0.15			This work
Physical Parameters				
	Spec. Synth.	SED fit	Emp. Rel.	
$M_*$ ( $M_\odot$ )			0.2843 $\pm$ 0.0065	This work
$R_*$ ( $R_\odot$ )		0.3159 <sup>+0.0036</sup> <sub>-0.0047</sub>	0.3105 $\pm$ 0.0089	This work
$L_*$ ( $L_\odot$ )		0.01020 <sup>+0.00014</sup> <sub>-0.00012</sub>		This work
$\rho_*$ ( $\rho_\odot$ )			9.5 $\pm$ 0.8	This work
Magnitudes				
$V$ (mag)	15.39 $\pm$ 0.20			(3)
$G$ (mag)	13.7390 $\pm$ 0.0029			(1)
$TESS$ (mag)	12.4934 $\pm$ 0.0075			(3)
$J$ (mag)	10.925 $\pm$ 0.019			(4)
$H$ (mag)	10.332 $\pm$ 0.019			(4)
$K_s$ (mag)	10.089 $\pm$ 0.020			(4)

**Notes.** <sup>(a)</sup> References: (1) Gaia EDR3 (Gaia Collaboration et al. 2021), (2) Bailer-Jones et al. (2021), (3) TIC v8.2 (Stassun et al. 2019), (4) 2MASS (Skrutskie et al. 2006).

<sup>(b)</sup> The error bars accounts for the random error from the fitting procedure. A systematic error of  $\sim 100$  K is associated with the absolute calibration of the instruments.

the contaminating flux comes from only one blended star, except for the TESS observations, due to the significantly larger pixel scale of TESS compared to that of ground-based detectors. The planet self-blend effect is negligible in the analysed datasets (Kipping & Tinetti 2010; Martin-Lagarde et al. 2020). Both  $F_*$  and  $F_c$  were computed through ExoTETHyS<sup>6</sup> (Morello et al. 2021), based on a precomputed grid of PHOENIX stellar spectra (Claret 2018). We fitted the photospheric parameters of the contaminating star ( $T_{c,\text{eff}}$  and  $\log g_c$ ), a flux scaling factor ( $f_c$ ) to account for, e.g., different distances of the target and contaminating stars, and an independent blend TESS factor ( $\beta_{TESS}$ ).

#### 4.2. Baseline models

In addition to planetary transit and possible third light contamination, other signals are present in the observed light-curves, both of astrophysical and instrumental origin. We modelled the modulations present in the TESS time series by using Gaussian Processes (GPs), which provide a flexible non-parametric method to approximate stochastic trends in various types of datasets (Rasmussen & Williams 2006; Roberts et al. 2012). In

the field of Astrophysics, GPs are often used to filter out stellar variability and instrumental systematic effects in photometric time series (Gibson et al. 2012; Evans et al. 2015; Barros et al. 2020). In this paper, we computed the TESS GPs using *celerite*<sup>7</sup> (Foreman-Mackey et al. 2017) with the Matern-3/2 kernel:

$$k(\tau) = \sigma_{\text{GP}}^2 \left[ \left( 1 + \frac{1}{\epsilon} \right) e^{-(1-\epsilon)\sqrt{3}\tau/\rho_{\text{GP}}} + \left( 1 - \frac{1}{\epsilon} \right) e^{-(1+\epsilon)\sqrt{3}\tau/\rho_{\text{GP}}} \right], \quad (3)$$

where  $\tau = |t_i - t_j|$  is the time interval between two points,  $\epsilon = 0.01$ ,  $\sigma_{\text{GP}}$  and  $\rho_{\text{GP}}$  are characteristic amplitude and timescale of the modulations. The choice of GP Matern-3/2 kernel has proven effective to detrend TESS photometry (e.g., González-Álvarez et al. 2021; Kossakowski et al. 2021; Murgas et al. 2021).

We detrended the ground-based light-curves by fitting linear models with maximum two auxiliary parameters, as detailed in Table 3.

<sup>6</sup> <https://github.com/ucl-exoplanets/ExoTETHyS>

**Table 2.** Stellar properties of TOI-2445.

Parameter	Value			Reference <sup>a</sup>
Astrometric Parameters				
$\alpha$ (epoch 2016.0)	02:53:15.8792			(1)
$\delta$ (epoch 2016.0)	+00:03:08.400			(1)
$\mu_\alpha$ (mas/yr)	$57.557 \pm 0.029$			(1)
$\mu_\delta$ (mas/yr)	$-23.693 \pm 0.025$			(1)
Parallax (mas)	$20.361 \pm 0.032$			(1)
Distance (pc)	$48.968 \pm 0.077$			(2)
Photospheric Parameters				
	Spec. Synth.	SED fit	Emp. Rel.	
$T_{*,\text{eff}}$ (K) <sup>b</sup>	$3375 \pm 10$	$3238^{+34}_{-25}$		This work
$\log g_*$ (dex)		$5.24^{+0.20}_{-0.40}$	$4.96 \pm 0.03$	This work
$[M/H]_*$ (dex)	$-0.32 \pm 0.07$	$-0.34 \pm 0.07$		This work
$[Fe/H]_*$ (dex)	$-0.39 \pm 0.16$			This work
Physical Parameters				
	Spec. Synth.	SED fit	Emp. Rel.	
$M_*$ ( $M_\odot$ )			$0.2448 \pm 0.0056$	This work
$R_*$ ( $R_\odot$ )		$0.2762^{+0.0055}_{-0.0051}$	$0.2699 \pm 0.0078$	This work
$L_*$ ( $L_\odot$ )		$0.00760^{+0.00019}_{-0.00017}$		This work
$\rho_*$ ( $\rho_\odot$ )			$12.5 \pm 1.1$	This work
Magnitudes				
$V$ (mag)	$15.69 \pm 0.03$			(3)
$G$ (mag)	$14.3977 \pm 0.0006$			(1)
$TESS$ (mag)	$13.1292 \pm 0.0076$			(3)
$J$ (mag)	$11.555 \pm 0.023$			(4)
$H$ (mag)	$11.033 \pm 0.022$			(4)
$K_s$ (mag)	$10.779 \pm 0.019$			(4)

**Notes.** <sup>(a)</sup> References: (1) Gaia EDR3 (Gaia Collaboration et al. 2021), (2) Bailer-Jones et al. (2021), (3) TIC v8.2 (Stassun et al. 2019), (4) 2MASS (Skrutskie et al. 2006).

<sup>(b)</sup> The error bars accounts for the random error from the fitting procedure. A systematic error of  $\sim 100$  K is associated with the absolute calibration of the instruments.

### 4.3. Bayesian priors

We made use of the *emcee* package to compute the posterior probability distributions of the astrophysical parameters associated with the contaminated transit models (Section 4.1), along with those of the data detrending parameters (Section 4.2). The prior distributions were chosen to discard unphysical solutions, and considering our knowledge of the system from ancillary observations, e.g., the stellar spectra. Table 4 reports the bayesian priors for all parameters.

We selected uniform priors on the radius ratio and total transit duration to let them be fully constrained by the transit light-curves themselves. These parameters were shared by all observations and passbands; second-order effects such as the wavelength-dependent absorption of the planetary atmospheres and possible changes in orbital inclinations were neglected. We also assumed linear ephemeris with gaussian priors on the orbital period and epoch of transits, centered on the ExoFOP values, but their  $\sigma$  widths were conservatively enhanced by a factor of 3. For the stellar mean density, we used our estimates from empirical relations (Tables 1 and 2) with a factor of 1.5 on the error bars.

The orbital eccentricity was fixed to zero, as is expected for USP planets.

The stellar LDCs were computed with ExoTETHyS (Morello et al. 2020b,a), based on the photospheric parameters reported in Tables 1 and 2, then transformed into  $q_1$  and  $q_2$  (see Section 4.1). We adopted broad gaussian priors centered on the theoretical values of  $q_1$  and  $q_2$  with widths  $\sigma = 0.1$ , that largely encompass all plausible values derived from stellar models with consistent photospheric parameters.

To compute the physical contamination model, we fixed the effective temperature and surface gravity of the target star, and assumed uniform priors for all the contaminant parameters, including the blend TESS factor. Finally, we selected uninformative prior distributions for all data detrending parameters and normalisation factors. In particular, we adopted log-uniform priors for the TESS GP parameters, that were shared over all sectors for the same target. The final *emcee* fit for TOI-1442 had 68 parameters, 150 walkers and 300000 iterations. The final *emcee* fit for TOI-2445 had 48 parameters, 110 walkers and 300000 iterations.

<sup>7</sup> <https://github.com/dfm/celerite>

**Table 3.** List of ground-based observations and auxiliary parameters used for detrending.

Target	Instrument	UT Date	Passband	Detrending
TOI-1442	MuSCAT3	2021 May 05	<i>r</i>	AIRMASS
TOI-1442	MuSCAT3	2021 May 05	<i>i</i>	AIRMASS
TOI-1442	MuSCAT3	2021 May 05	$z_s$	AIRMASS
TOI-1442	MuSCAT3	2021 Jun 06	<i>r</i>	tot_C_cnts
TOI-1442	MuSCAT3	2021 Jun 06	<i>i</i>	tot_C_cnts
TOI-1442	MuSCAT3	2021 Jun 06	$z_s$	width_T1
TOI-1442	MuSCAT3	2021 Jun 17	<i>g</i>	AIRMASS
TOI-1442	MuSCAT3	2021 Jun 17	<i>r</i>	width_T1
TOI-1442	MuSCAT3	2021 Jun 17	<i>i</i>	AIRMASS
TOI-1442	MuSCAT3	2021 Jun 17	$z_s$	AIRMASS
TOI-1442	LCO-McD-1m0	2020 Aug 14	<i>i</i>	AIRMASS
TOI-1442	LCO-McD-1m0	2020 Aug 30	<i>I</i>	–
TOI-1442	LCO-McD-1m0	2020 Sep 26	<i>i</i>	BJD_TDB, Sky/Pixel_T1
TOI-1442	LCO-McD-1m0	2020 Oct 21	<i>i</i>	AIRMASS
TOI-1442	PESTO	2020 Feb 09	<i>i</i>	AIRMASS
TOI-2445	MuSCAT	2021 Feb 07	<i>g</i>	BJD_TDB, AIRMASS
TOI-2445	MuSCAT	2021 Feb 07	<i>r</i>	BJD_TDB, AIRMASS
TOI-2445	MuSCAT	2021 Feb 07	$z_s$	BJD_TDB, AIRMASS
TOI-2445	MuSCAT2	2021 Aug 06	<i>g</i>	–
TOI-2445	MuSCAT2	2021 Aug 06	<i>r</i>	–
TOI-2445	MuSCAT2	2021 Aug 06	<i>i</i>	–
TOI-2445	MuSCAT2	2021 Aug 06	$z_s$	–
TOI-2445	MuSCAT2	2021 Sep 14	<i>g</i>	–
TOI-2445	MuSCAT2	2021 Sep 14	<i>i</i>	–
TOI-2445	MuSCAT2	2021 Sep 14	$z_s$	–
TOI-2445	TRAPPIST-S	2021 Jan 08	$I + z$	–
TOI-2445	TRAPPIST-S	2021 Jan 14	$I + z$	–
TOI-2445	MLO-Lewin-0m36	2021 Jan 10	<i>I</i>	AIRMASS, Y(FITS)_T1

## 5. Radial velocity analysis

We fitted the IRD RV data using `radvel`<sup>8</sup> (Fulton et al. 2018). We adopted gaussian priors on the orbital period and epoch of transits, based on the results of the photometric analysis reported in Table 5, and uniform prior with upper bound of  $300 \text{ m s}^{-1}$  on the RV semiamplitude ( $K_p$ ). We also included the jitter term with uniform prior between 0 and 100. However, the best-fit models do not provide a good match to the observed RV data, as it can be seen in Figure 3. Alternative configurations with a linear trend do not provide significant improvements.

There are at least three possible explanations of such a poor agreement between the RV data and our simple RV models. First, the RV measurements can be dominated by systematic effects, as their overall ranges of variations are comparable with the potential instrumental offsets of  $\sim 10 \text{ m s}^{-1}$ . Second, strong stellar activity could also cause similar offsets. The third and most intriguing scenario is that TOI-1442 and/or TOI-2445 host additional planets with detectable RV signals, but which are not transiting. More RV measurements are required to test these different scenarios.

Nonetheless, the current RV measurements have a good phase coverage, so that we can constrain  $K_p$ . We derive  $3\sigma$  upper limits as half of the variation ranges obtained by subtracting the maximum value plus three times its upper error bar and the minimum value minus three times its lower error bar.

## 6. Results

### 6.1. TOI-1442 b

Figure 4 shows the TESS phase-folded light-curve and ground-based light-curves, after data detrending, and best-fit contaminated transit models for TOI-1442 b. Figure 5 shows the posterior distributions and mutual correlations of the transit model parameters. The multiband light-curve analysis constrains the  $T_{c,\text{eff}}$  of a hypothetical blended source to similar or cooler values than  $T_{*,\text{eff}}$ . The posterior distribution of  $T_{c,\text{eff}}$  is bimodal with a primary peak towards the lower temperature limit of the PHOENIX stellar models grid (2300 K), and a second peak at  $T_{c,\text{eff}} \sim 3000 \text{ K}$ . Overall, we pose a  $3\sigma$  upper limit at  $T_{c,\text{eff}} < 4770 \text{ K}$ . If such a blend exists, it would not imprint a significant colour-dependent signature, and the dilution factor would be nearly uniform over all passbands. We checked that the differential third light fraction

$$\Delta\beta_{\text{pass}} = \beta_{\text{pass}} - \beta_{z_s}, \quad (4)$$

with  $\beta$  defined as in Equation 1, is consistent with zero within  $1.3\sigma$  (1-10%) for all passbands, including TESS.

The radius ratio turns out to be  $p = 0.0374^{+0.0042}_{-0.0025}$  with a  $3\sigma$  upper limit at  $p < 0.0749$ . Multiplying these values by  $R_*$  from Table 1, the radius of the planetary candidate is  $R_p = 1.27^{+0.50}_{-0.44} R_\oplus$  with a  $3\sigma$  upper limit at  $R_p < 2.76 R_\oplus$ . The small size of the transiting object around TOI-1442 inferred by multicolour photometry confirms that it must be planetary in nature, and classifies it as either a super-Earth or a mini-Neptune. Note that the error bars on the planetary radius are dominated by those on the

<sup>8</sup> <https://github.com/California-Planet-Search/radvel>

**Table 4.** Prior probability distributions of the fitted parameters.

	Parameter	TOI-1442	TOI-2445
Transit	$p$	$\mathcal{U}(0, 1)$	$\mathcal{U}(0, 1)$
	$P$ (d) <sup>a</sup>	$\mathcal{N}(0.409072, 0.000011)$	$\mathcal{N}(0.371133, 0.000047)$
	$T_0$ (BTJD) <sup>a</sup>	$\mathcal{N}(1683.45058, 0.00085)$	$\mathcal{N}(1411.21732, 0.00188)$
	$\rho_*$ ( $\rho_\odot$ )	$\mathcal{N}(9.50, 1.27)$	$\mathcal{N}(12.45, 1.67)$
	$T_{14}$ (hr) <sup>a</sup>	$\mathcal{U}(0.169, 1.036)$	$\mathcal{U}(0, 1.289)$
Contamination	$T_{*,\text{eff}}$ (K) <sup>b</sup>	3304	3306
	$\log g_*$ (dex) <sup>c</sup>	4.91	4.96
	$T_{c,\text{eff}}$ (K)	$\mathcal{U}(2300, 12000)$	$\mathcal{U}(2300, 12000)$
	$\log g_c$ (dex)	$\mathcal{U}(2.0, 5.5)$	$\mathcal{U}(2.0, 5.5)$
	$f_c$ <sup>d</sup>	$\mathcal{U}(-1, 1000)$	$\mathcal{U}(-1, 1000)$
	$\beta_{TESS}$ <sup>d</sup>	$\mathcal{U}(-0.2, 0.99)$	$\mathcal{U}(-0.2, 0.99)$
LDCs <sup>e</sup>	$q_{1,TESS}$	$\mathcal{N}(0.038667, 0.1) \times \mathcal{U}(0, 1)$	$\mathcal{N}(0.038237, 0.1) \times \mathcal{U}(0, 1)$
	$q_{2,TESS}$	$\mathcal{N}(0.005047, 0.1) \times \mathcal{U}(0, 1)$	$\mathcal{N}(0.00067, 0.1) \times \mathcal{U}(0, 1)$
	$q_{1,g}$	$\mathcal{N}(0.104994, 0.1) \times \mathcal{U}(0, 1)$	$\mathcal{N}(0.104916, 0.1) \times \mathcal{U}(0, 1)$
	$q_{2,g}$	$\mathcal{N}(0.0, 0.1) \times \mathcal{U}(0, 1)$	$\mathcal{N}(0.0, 0.1) \times \mathcal{U}(0, 1)$
	$q_{1,r}$	$\mathcal{N}(0.126307, 0.1) \times \mathcal{U}(0, 1)$	$\mathcal{N}(0.123358, 0.1) \times \mathcal{U}(0, 1)$
	$q_{2,r}$	$\mathcal{N}(0.102417, 0.1) \times \mathcal{U}(0, 1)$	$\mathcal{N}(0.092309, 0.1) \times \mathcal{U}(0, 1)$
	$q_{1,i}$	$\mathcal{N}(0.047087, 0.1) \times \mathcal{U}(0, 1)$	$\mathcal{N}(0.047093, 0.1) \times \mathcal{U}(0, 1)$
	$q_{2,i}$	$\mathcal{N}(0.0, 0.1) \times \mathcal{U}(0, 1)$	$\mathcal{N}(0.0, 0.1) \times \mathcal{U}(0, 1)$
	$q_{1,z_s}$	$\mathcal{N}(0.031820, 0.1) \times \mathcal{U}(0, 1)$	$\mathcal{N}(0.031817, 0.1) \times \mathcal{U}(0, 1)$
	$q_{2,z_s}$	$\mathcal{N}(0.0, 0.1) \times \mathcal{U}(0, 1)$	$\mathcal{N}(0.0, 0.1) \times \mathcal{U}(0, 1)$
	$q_{1,l}$	$\mathcal{N}(0.028676, 0.1) \times \mathcal{U}(0, 1)$	$\mathcal{N}(0.028667, 0.1) \times \mathcal{U}(0, 1)$
	$q_{2,l}$	$\mathcal{N}(0.0, 0.1) \times \mathcal{U}(0, 1)$	$\mathcal{N}(0.0, 0.1) \times \mathcal{U}(0, 1)$
	$q_{1,l+z}$	–	$\mathcal{N}(0.022097, 0.1) \times \mathcal{U}(0, 1)$
	$q_{2,l+z}$	–	$\mathcal{N}(0.0, 0.1) \times \mathcal{U}(0, 1)$
Baseline	$\log_{10} \sigma_{\text{GP}}$	$\mathcal{U}(-10, 6)$	$\mathcal{U}(-10, 6)$
	$\log_{10} \rho_{\text{GP}}$	$\mathcal{U}(-10, 6)$	$\mathcal{U}(-10, 6)$
	$N_{TESS}$ <sup>f</sup>	$\mathcal{U}(1000, 2000)$	$\mathcal{U}(400, 1400)$
	$N_{\text{ground}}$ <sup>f</sup>	$\mathcal{U}(0.5, 1.5)$	$\mathcal{U}(0.5, 1.5)$
	$X_1, X_2$ <sup>g</sup>	$\mathcal{U}(-1, 1)$	$\mathcal{U}(-1, 1)$

**Notes.**  $\mathcal{U}(a, b)$  denotes a uniform prior delimited by  $a$  and  $b$ ;  $\mathcal{N}(\mu, \sigma)$  denotes a normal prior with  $\mu$  mean and  $\sigma$  width.

<sup>(a)</sup> Centered on the ExoFOP values as of 2021 November 30. For the normal distributions, the prior  $\sigma$  equals three times the nominal error bars. For the uniform distributions, the whole interval equals six times the nominal error bars.

<sup>(b)</sup> Arithmetic average between spectral synthesis and SED fitting estimates from Tables 1 and 2.

<sup>(c)</sup> Obtained with empirical relations, from Tables 1 and 2.

<sup>(d)</sup> Negative contamination values are allowed to avoid bouncing effect at the physical boundary of zero contaminants; they could also be caused by systematic offsets.

<sup>(e)</sup> Some ground-based detectors share the same LDCs, if they have the same passband (see Table 3).

<sup>(f)</sup> Normalisation factors, i.e., multiplicative factors for the contaminated transit models. A factor is fitted for each TESS sector and for each ground-based observation.

<sup>(g)</sup> Coefficients of the linear detrending models for ground-based observation, using up to two auxiliary parameters (see Table 3).

stellar radius, hence they cannot be significantly reduced by observing more transit light-curves.

We estimated the equilibrium temperature to be  $T_{p,\text{eq}} = 1359^{+49}_{-42}$  K, assuming zero albedo and no heat redistribution. The equilibrium temperature is above the 880 K to melt rocks and metals on the surface of the dayside hemisphere (McArthur et al. 2004).

From the RV measurements, we derived a  $3\sigma$  upper limit of  $K_p < 34 \text{ m s}^{-1}$ . Using  $M_*$  from Table 1, we infer a  $3\sigma$  upper limit on the (projected) planet mass of  $M_p \sin i \approx M_p < 18 M_\oplus$ .

## 6.2. TOI-2445 b

Figure 6 shows the TESS phase-folded light-curve and ground-based light-curves, after data detrending, and best-fit contaminated transit models for TOI-2445 b. Figure 7 shows the posterior distributions and mutual correlations of the transit model

parameters. The multiband light-curve analysis led to similar results on the possible blend for this target. The posterior distribution of  $T_{c,\text{eff}}$  is bimodal with two similar peaks towards the lower temperature limit of 2300 K and at  $\sim 3500$  K. Overall, we pose a  $3\sigma$  upper limit at  $T_{c,\text{eff}} < 5760$  K. The differential third light fraction is within less than  $1\sigma$  (1-10%) for all passbands.

The radius ratio is  $p = 0.052^{+0.039}_{-0.007}$  with a  $3\sigma$  upper limit at  $p < 0.240$ . Multiplying these values by  $R_*$  from Table 2, the radius of the planetary candidate is  $R_p = 1.52^{+1.20}_{-0.26} R_\oplus$  with  $3\sigma$  upper limit at  $R_p < 7.69 R_\oplus$  (equivalent to  $R_p < 0.69 R_J$ ). The small size of the transiting object around TOI-2445 inferred by multicolour photometry confirms that it must be planetary in nature, and it is likely to be another super-Earth or mini-Neptune. However, it could also be a giant planet, given the  $3\sigma$  upper limit on its radius. Differently from TOI-1442 b, the error bars on the planetary radius are dominated by those on the photometric ra-

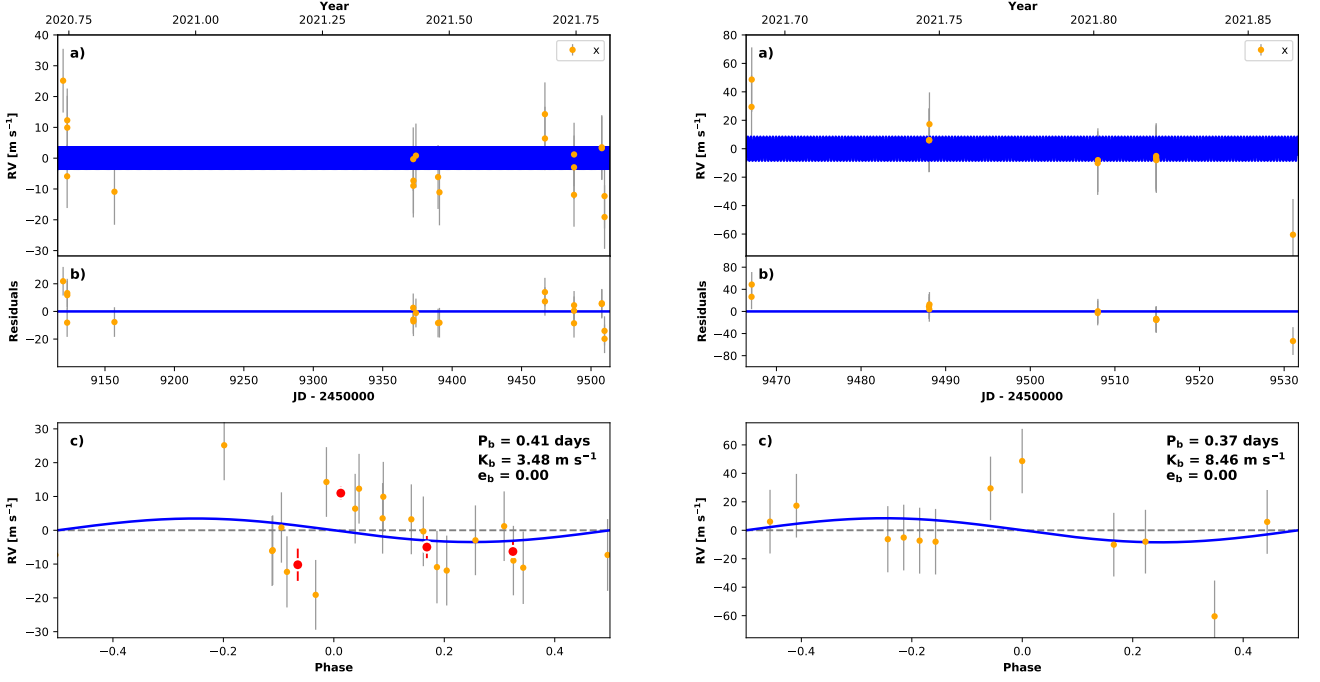


**Fig. 3.** RV data and best-fit `radvel` models for TOI-1442 (left) and TOI-2445 (right). The top panels display the full timeline data, while the bottom panels show the phase-folded data using the best-fit orbital parameters. The error bars do not account for systematic offsets.

**Table 5.** Final system parameters

	Parameter	TOI-1442	TOI-2445
Stellar	$T_{*,\text{eff}}$ (K)	$3304 \pm 50$	$3306 \pm 75$
	$\log g_*$ (dex)	$4.91 \pm 0.03$	$4.96 \pm 0.03$
	$[M/H]_*$ (dex)	$0.11 \pm 0.07$	$-0.33 \pm 0.07$
	$[Fe/H]_*$ (dex)	$0.03 \pm 0.15$	$-0.39 \pm 0.16$
	$M_*$ ( $M_\odot$ )	$0.2843 \pm 0.0065$	$0.2448 \pm 0.0056$
	$R_*$ ( $R_\odot$ )	$0.3105 \pm 0.0089$	$0.2699 \pm 0.0078$
	$L_*$ ( $L_\odot$ )	$0.01020^{+0.00014}_{-0.00012}$	$0.00760^{+0.00019}_{-0.00017}$
Transit fit	$p$	$0.0374^{+0.0042}_{-0.0025}$	$0.052^{+0.039}_{-0.007}$
	$P$ (d)	$0.4090682 \pm 0.0000004$	$0.3711286 \pm 0.0000004$
	$T_0$ (BJJD)	$1683.45192^{+0.00033}_{-0.00036}$	$1411.21989^{+0.00076}_{-0.00086}$
	$\rho_*$ ( $\rho_\odot$ )	$9.02^{+0.89}_{-1.05}$	$12.4 \pm 1.6$
	$T_{14}$ (hr)	$0.650 \pm 0.016$	$0.549^{+0.029}_{-0.024}$
(derived)	$a/R_*^a$	$4.83^{+0.15}_{-0.20}$	$5.03^{+0.21}_{-0.23}$
	$b^b$	$0.29 \pm 0.13$	$0.44^{+0.10}_{-0.13}$
	$i$ (deg) <sup>c</sup>	$86.59^{+1.57}_{-1.70}$	$84.97^{+1.59}_{-1.35}$
RVs	$K_p$ ( $\text{m s}^{-1}$ )	$< 34$	$< 82$
Planetary and orbital (derived)	$R_p$ ( $R_\oplus$ )	$1.27^{0.50}_{-0.44}$	$1.52^{1.20}_{-0.26}$
	$M_p$ ( $M_\oplus$ )	$< 18$	$< 38$
	$a$ (au) <sup>d</sup>	$0.00697^{+0.00042}_{-0.00048}$	$0.00632^{+0.00044}_{-0.00047}$
	$T_{p,\text{eq}}$ (K) <sup>e</sup>	$1359^{+49}_{-42}$	$1332^{+61}_{-57}$

**Notes.** Values preceded by  $<$  report  $3\sigma$  upper limits.

(a) Orbital semimajor axis relative in units of the stellar radius.

(b) Impact parameter.

(c) Orbital inclination.

(d) Orbital semimajor axis.

(e) Dayside equilibrium temperature, assuming zero albedo and no heat redistribution.

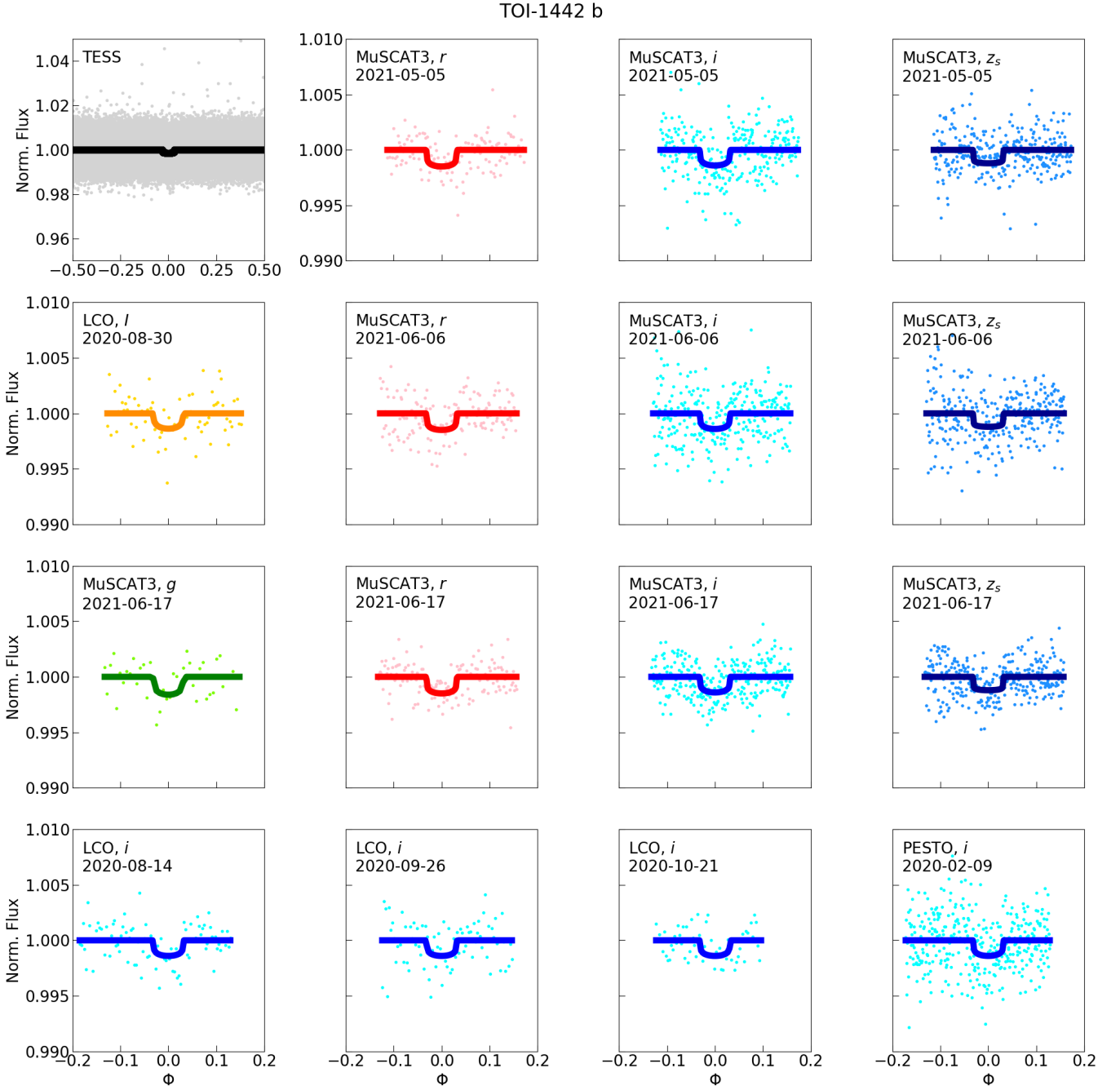


**Fig. 4.** TESS phase-folded light-curve and ground-based light-curves, after data detrending, and best-fit contaminated transit models for TOI-1442 b.

dus ratio, and hence they could be reduced by observing more transits.

We estimated the equilibrium temperature to be  $T_{p,eq} = 1332_{-57}^{+61}$ , which is also pointing to a dayside hemisphere covered by molten rocks and metals.

From the RV measurements, we derived a  $3\sigma$  upper limit of  $K_p < 82 \text{ m s}^{-1}$ . Using  $M_*$  from Table 2, we infer a  $3\sigma$  upper limit on the (projected) planet mass of  $M_p \sin i \approx M_p < 38 M_\oplus$ .

## 7. Discussion

Figure 8 shows the radius vs. orbital period distribution of the known USP planets. TOI-1442 b and TOI-2445 b are among

the 12 confirmed USP planets with the shortest orbital periods, and likewise their radii are smaller than  $2R_\oplus$ . If we consider the known sample of 13 USP planets around M dwarfs, TOI-1442 b and TOI-2445 b have the third and the fifth shortest periods, respectively. They also have the fourth and fifth highest equilibrium temperatures. All the USP planets around M dwarfs have radii smaller than  $2R_\oplus$ , except K2-22 b (Sanchis-Ojeda et al. 2015). The mass upper limits of  $M_p < 18 M_\oplus$  for TOI-1442 b and  $M_p < 38 M_\oplus$  for TOI-2445 b confirm the sub-giant nature. More RV measurements are desirable to place significant constraints on their masses and mean densities, hence their chemical compositions.

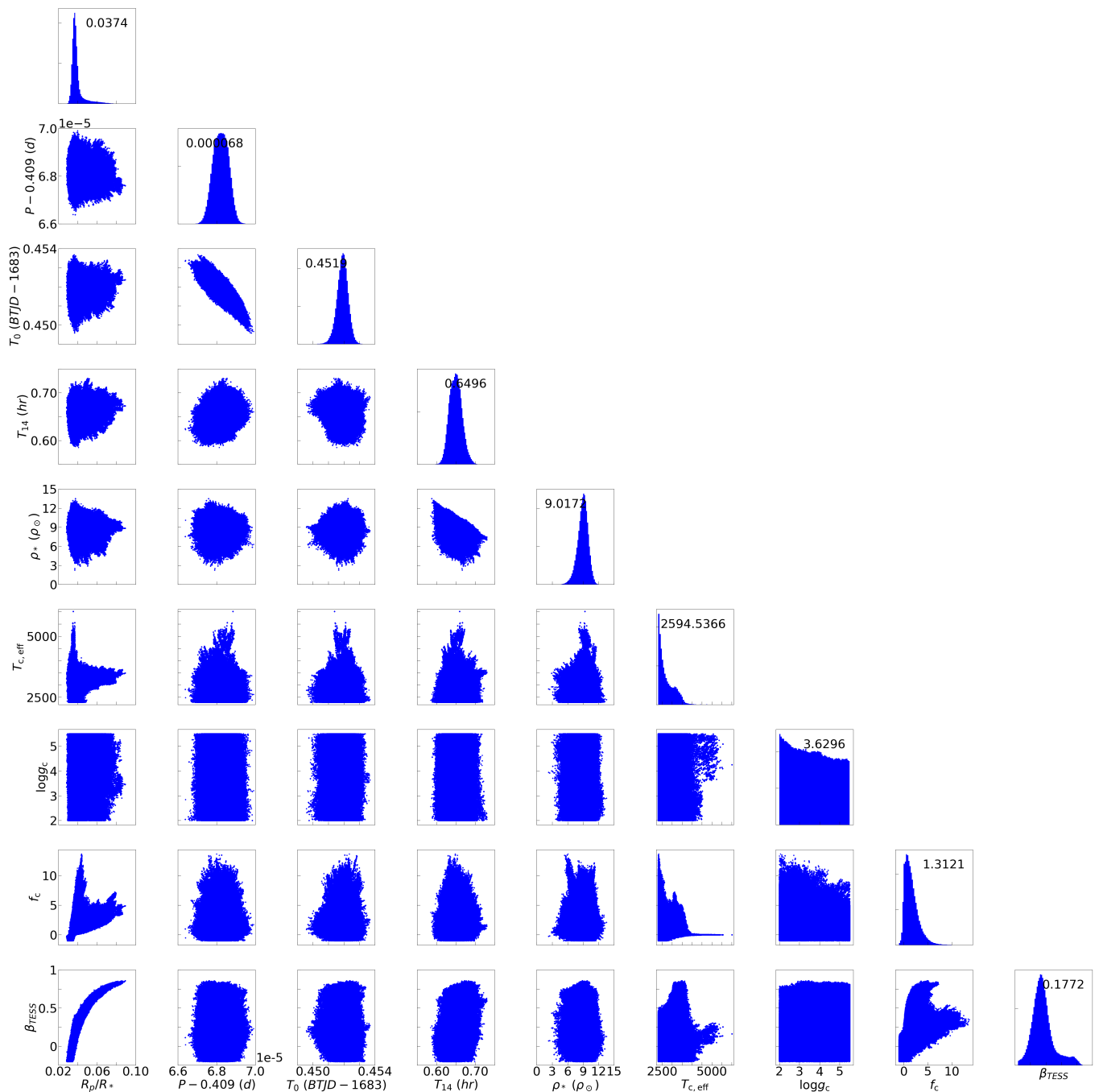


**Fig. 5.** Cornerplot showing the posterior distributions and mutual correlations of the transit model parameters for TOI-1442.

The dispersion in our RV measurements suggests the possible presence of additional non-transiting planets around both stars, although stellar activity or instrumental systematic offsets could also provide alternative explanations. Despite only a small fraction of USP planets have been detected in multiplanet systems, four out of the 11 USP planets previously reported around M dwarfs are members of multiplanet systems. These systems are Kepler-42 (Muirhead et al. 2012), LTT-3780 (Cloutier et al. 2020), LHS-1678 (Silverstein et al. 2021) and LP 791-18 (Crossfield et al. 2019). Another peculiarity of the four M dwarf systems with an USP planets, is that their orbits are aligned so that the outer planets are also transiting. The only non-transiting planet discovered in these systems is LHS-1678 d, which has

a wide orbit with a period of decades. The new RV measurements will also be useful to assess the architecture of the planetary systems around TOI-1442 and TOI-2445, which is important to validate formation theories for USP planets around M dwarfs and differences with those around later-type stars (e.g., Petrovich et al. 2020).

Currently, neither TOI-1442 b or TOI-2445 b are suitable targets for atmospheric characterisation, mostly due to the faintness of their host stars. However, this might change if the minimum masses of the planets are determined to be at the lower end of the current uncertainty range.

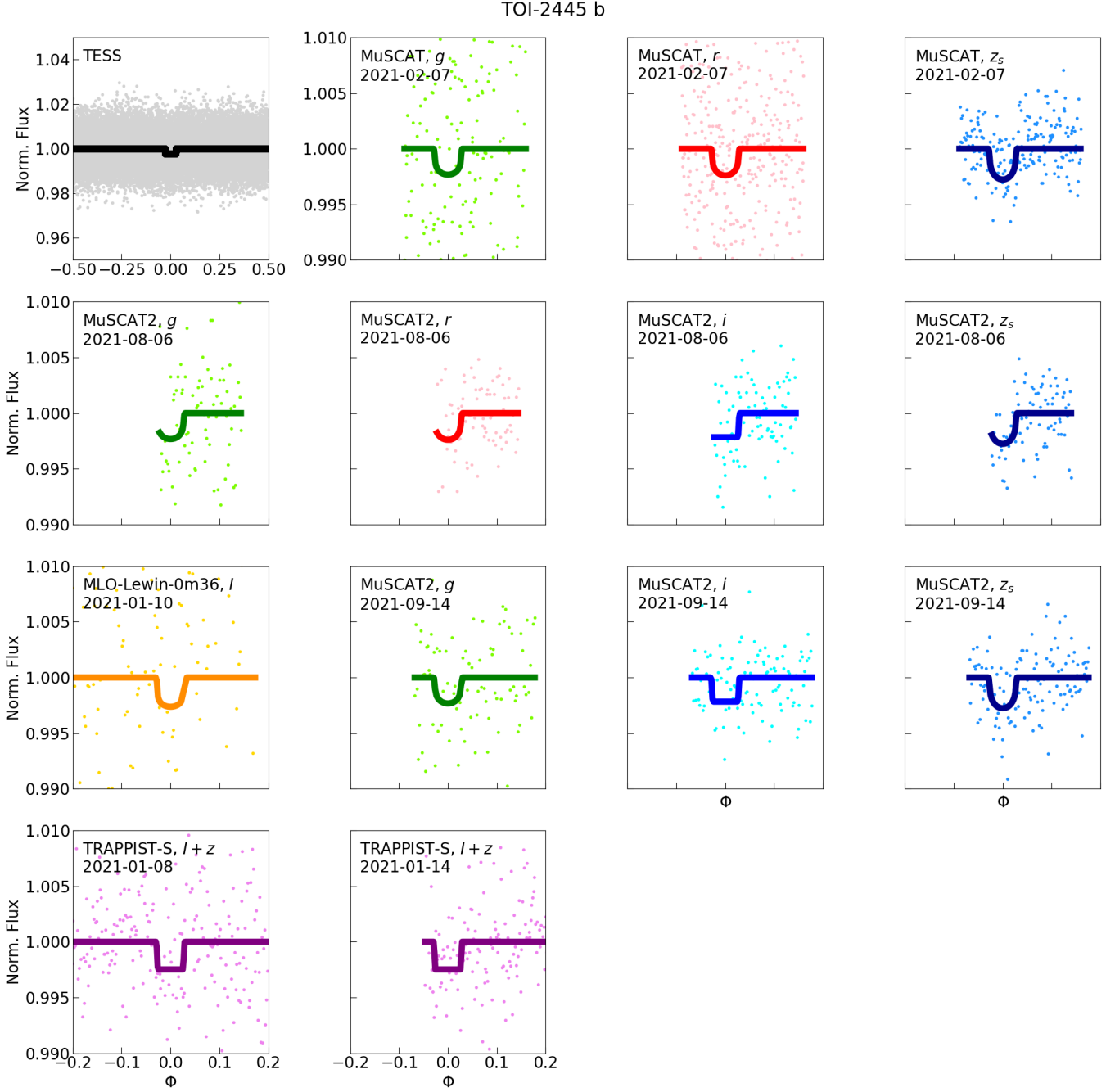


**Fig. 6.** TESS phase-folded light-curve and ground-based light-curves, after data detrending, and best-fit contaminated transit models for TOI-2445 b.

## 8. Conclusions

We confirm the planetary nature of TOI-1442 b and TOI-2445 b, two USP planets with M dwarf stellar hosts. TOI-1442 b has an orbital period of  $P = 0.4090682 \pm 0.0000004 d$ , a radius of  $R_p = 1.27^{+0.50}_{-0.44} R_\oplus$ , and equilibrium temperature of  $T_{p,eq} = 1359^{+49}_{-42} K$ . TOI-2445 b has an orbital period of  $P = 0.3711286 \pm 0.0000004 d$ , a radius of  $R_p = 1.52^{+1.20}_{-0.26} R_\oplus$ , and equilibrium temperature of  $T_{p,eq} = 1332^{+61}_{-57} K$ . We also report  $3\sigma$  upper limits on their masses of  $M_p < 18 M_\oplus$  and  $M_p < 38 M_\oplus$ , respectively.

These are interesting targets to follow-up with high-precision RV facilities to improve their mass measurements (to constrain

their bulk compositions) and possibly detect other planetary companions.

*Acknowledgements.* G. M. has received funding from the European Union’s Horizon 2020 research and innovation programme under the Marie Skłodowska-Curie grant agreement No. 895525. This work is partly financed by the Spanish Ministry of Economics and Competitiveness through grants PGC2018-098153-B-C31. This work was partly supported by MEXT/JSPS KAKENHI Grant Numbers JP17H04574, JP18H05439, JP20J21872, JP18H05439, JP20K14521, JP20K14518, JP21K20376, JP21K13975, JP18H05439, JP18H05442, JP15H02063, JP22000005, JP18H05439, JP19K14783, JP21H00035, JST CREST Grant Number JPMJCR1761, Astrobiology Center SATELLITE Research project AB022006, and Astrobiology Center PROJECT Research AB031014. This research is partly based on data collected at Subaru Telescope, which is operated by the National Astronomical Observatory of Japan. We are honored and grateful for the opportunity to observe the universe from

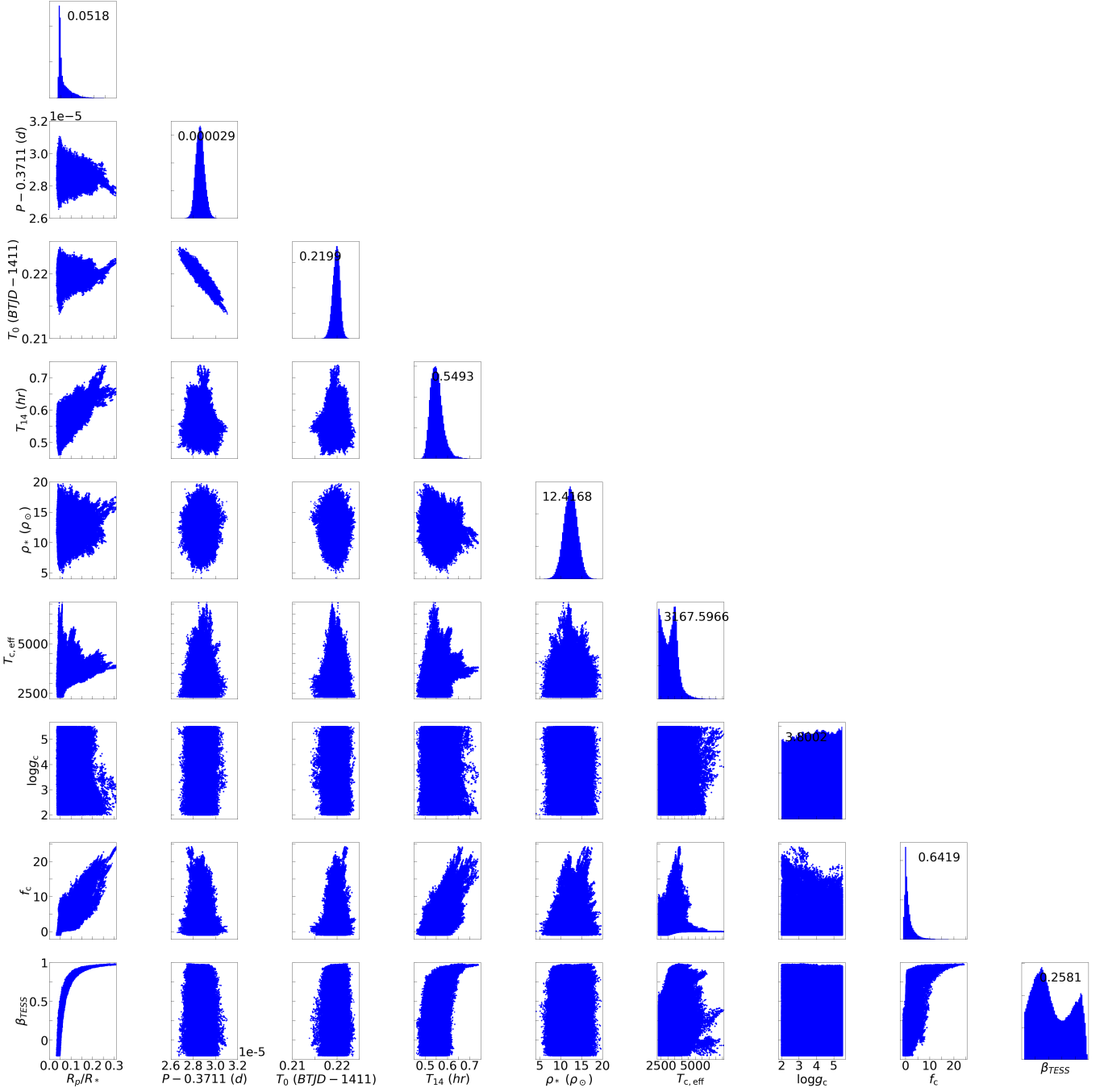


**Fig. 7.** Cornerplot showing the posterior distributions and mutual correlations of the transit model parameters for TOI-2445.

Maunakea, which has cultural, historical, and natural significance in Hawaii. The research leading to these results has received funding from the ARC grant for Concerted Research Actions, financed by the Wallonia-Brussels Federation. TRAPPIST is funded by the Belgian Fund for Scientific Research (Fond National de la Recherche Scientifique, FNRS) under the grant PDR T.0120.21. MG and EJ are F.R.S.-FNRS Senior Research Associate. This work makes use of observations from the LCOGT network. Part of the LCOGT telescope time was granted by NOIRLab through the Mid-Scale Innovations Program (MSIP). MSIP is funded by NSF. This paper is based on observations made with the MuSCAT3 instrument, developed by the Astrobiology Center and under financial supports by JSPS KAKENHI (JP18H05439) and JST PRESTO (JPMJPR1775), at Faulkes Telescope North on Maui, HI, operated by the Las Cumbres Observatory.

## References

- Allard, F. 2014, in *Exploring the Formation and Evolution of Planetary Systems*, ed. M. Booth, B. C. Matthews, & J. R. Graham, Vol. 299, 271–272
- Aller, A., Lillo-Box, J., Jones, D., Miranda, L. F., & Barceló Forteza, S. 2020, *A&A*, 635, A128
- Bailer-Jones, C. A. L., Rybizki, J., Foesneau, M., Demleitner, M., & Andrae, R. 2021, *AJ*, 161, 147
- Barros, S. C. C., Demangeon, O., Díaz, R. F., et al. 2020, *A&A*, 634, A75
- Brown, T. M., Baliber, N., Bianco, F. B., et al. 2013, *Publications of the Astronomical Society of the Pacific*, 125, 1031
- Chiang, E. & Laughlin, G. 2013, *MNRAS*, 431, 3444
- Claret, A. 2018, *A&A*, 618, A20
- Cloutier, R., Eastman, J. D., Rodriguez, J. E., et al. 2020, *AJ*, 160, 3
- Collins, K. A., Kielkopf, J. F., Stassun, K. G., & Hessman, F. V. 2017, *AJ*, 153, 77
- Crossfield, I. J. M., Waalkes, W., Newton, E. R., et al. 2019, *ApJ*, 883, L16

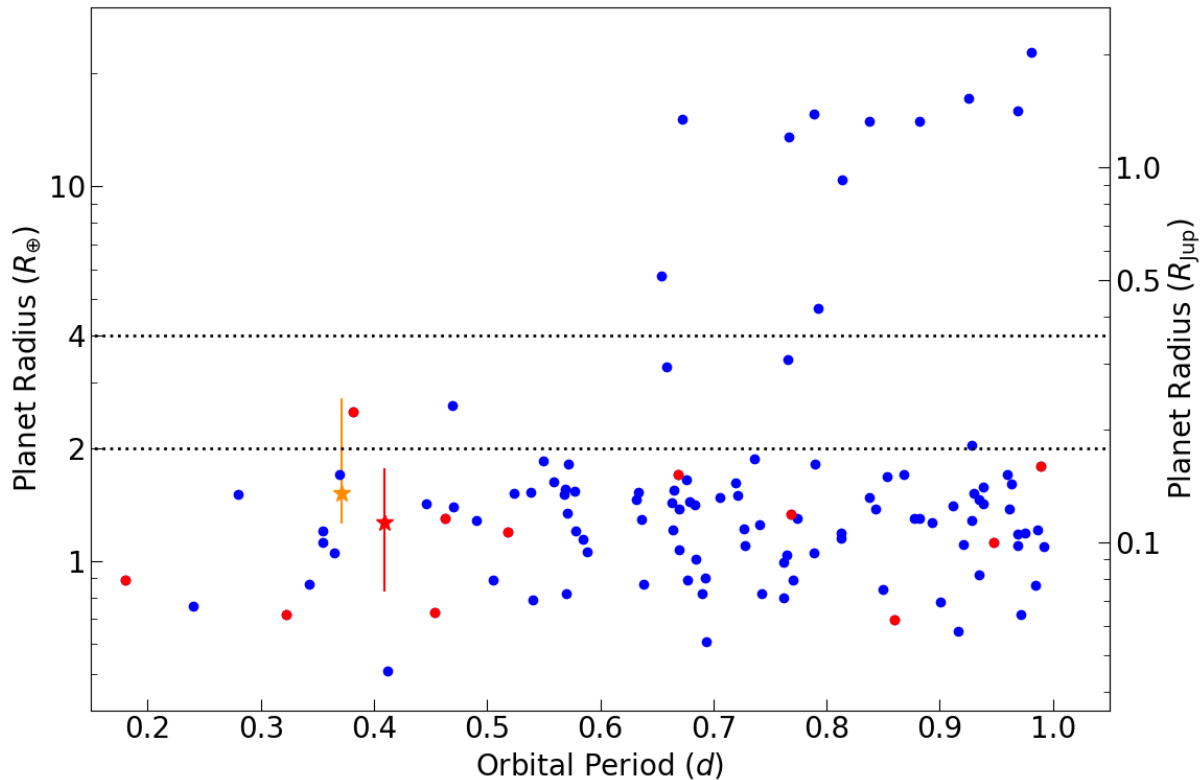


**Fig. 8.** Planetary radius vs. orbital period for the known USP planets, based on the same data of Figure 1. Planets around M dwarfs are colored in red. The red and orange stars correspond to TOI-1442 b and TOI-2445 b, based on the final results of our analysis.

- Cutri, R. M., Wright, E. L., Conrow, T., et al. 2021, *VizieR Online Data Catalog*, II/328
- Evans, T. M., Aigrain, S., Gibson, N., et al. 2015, *MNRAS*, 451, 680
- Fischer, D. A. & Valenti, J. 2005, *ApJ*, 622, 1102
- Foreman-Mackey, D., Agol, E., Ambikasaran, S., & Angus, R. 2017, *AJ*, 154, 220
- Foreman-Mackey, D., Hogg, D. W., Lang, D., & Goodman, J. 2013, *PASP*, 125, 306
- Fressin, F., Torres, G., Charbonneau, D., et al. 2013, *ApJ*, 766, 81
- Fukui, A., Narita, N., Tristram, P. J., et al. 2011, *PASJ*, 63, 287
- Fulton, B. J., Petigura, E. A., Blunt, S., & Sinukoff, E. 2018, *PASP*, 130, 044504
- Gaia Collaboration, Brown, A. G. A., Vallenari, A., et al. 2021, *A&A*, 649, A1
- Garcia, L. J., Timmermans, M., Pozuelos, F. J., et al. 2021, *MNRAS*[arXiv:2111.02814]
- Gaudi, B. S., Seager, S., & Mallen-Ornelas, G. 2005, *ApJ*, 623, 472
- Gibson, N. P., Aigrain, S., Roberts, S., et al. 2012, *MNRAS*, 419, 2683
- Gillon, M., Jehin, E., Magain, P., et al. 2011, *EPJ Web of Conferences*, 11, 06002
- González-Álvarez, E., Zapatero Osorio, M. R., Sanz-Forcada, J., et al. 2021, arXiv e-prints, arXiv:2111.14602
- Hestroffer, D. 1997, *A&A*, 327, 199
- Hirano, T., Kuzuhara, M., Kotani, T., et al. 2020, *PASJ*, 72, 93
- Howard, A. W., Marcy, G. W., Bryson, S. T., et al. 2012, *ApJS*, 201, 15
- Ishikawa, H. T., Aoki, W., Hirano, T., et al. 2022, *AJ*, 163, 72
- Ishikawa, H. T., Aoki, W., Kotani, T., et al. 2020, *PASJ*, 72, 102
- Jehin, E., Gillon, M., Queloz, D., et al. 2011, *The Messenger*, 145, 2
- Jenkins, J. M., Twicken, J. D., McCauliff, S., et al. 2016, in *Society of Photo-Optical Instrumentation Engineers (SPIE) Conference Series*, Vol. 9913, Software and Cyberinfrastructure for Astronomy IV, ed. G. Chiozzi & J. C. Guzman, 99133E
- Jensen, E. 2013, *Tapir: A web interface for transit/eclipse observability*
- Kipping, D. M. 2013, *MNRAS*, 435, 2152
- Kipping, D. M. & Tinetti, G. 2010, *MNRAS*, 407, 2589
- Königl, A., Giacalone, S., & Matsakos, T. 2017, *ApJ*, 846, L13
- Kossakowski, D., Kemmer, J., Bluhm, P., et al. 2021, *A&A*, 656, A124
- Kotani, T., Tamura, M., Nishikawa, J., et al. 2018, in *Society of Photo-Optical Instrumentation Engineers (SPIE) Conference Series*, Vol. 10702, Ground-based and Airborne Instrumentation for Astronomy VII, ed. C. J. Evans, L. Simard, & H. Takami, 1070211
- Lee, E. J. & Chiang, E. 2017, *ApJ*, 842, 40
- Lundkvist, M. S., Kjeldsen, H., Albrecht, S., et al. 2016, *Nature Communications*, 7, 11201
- Mann, A. W., Dupuy, T., Kraus, A. L., et al. 2019, *ApJ*, 871, 63
- Mann, A. W., Feiden, G. A., Gaidos, E., Boyajian, T., & von Braun, K. 2015, *ApJ*, 804, 64
- Martin-Lagarde, M., Morello, G., Lagage, P.-O., Gastaud, R., & Cossou, C. 2020, *AJ*, 160, 197
- Mayor, M. & Queloz, D. 1995, *Nature*, 378, 355
- McArthur, B. E., Endl, M., Cochran, W. D., et al. 2004, *ApJ*, 614, L81
- McCully, C., Volgenau, N. H., Harbeck, D.-R., et al. 2018, in *Society of Photo-Optical Instrumentation Engineers (SPIE) Conference Series*, Vol. 10707, Proc. SPIE, 107070K
- Morello, G., Claret, A., Martin-Lagarde, M., et al. 2020a, *The Journal of Open Source Software*, 5, 1834
- Morello, G., Claret, A., Martin-Lagarde, M., et al. 2020b, *AJ*, 159, 75
- Morello, G., Tsiaras, A., Howarth, I. D., & Homeier, D. 2017, *AJ*, 154, 111
- Morello, G., Zingales, T., Martin-Lagarde, M., Gastaud, R., & Lagage, P.-O. 2021, *AJ*, 161, 174
- Morris, R. L., Twicken, J. D., Smith, J. C., et al. 2020, *Kepler Data Processing Handbook: Photometric Analysis*, Kepler Science Document KSCI-19081-003
- Muirhead, P. S., Johnson, J. A., Apps, K., et al. 2012, *ApJ*, 747, 144
- Murgas, F., Astudillo-Defru, N., Bonfils, X., et al. 2021, *A&A*, 653, A60
- Narita, N., Fukui, A., Kusakabe, N., et al. 2015, *Journal of Astronomical Telescopes, Instruments, and Systems*, 1, 045001
- Narita, N., Fukui, A., Kusakabe, N., et al. 2019, *Journal of Astronomical Telescopes, Instruments, and Systems*, 5, 015001
- Narita, N., Fukui, A., Yamamuro, T., et al. 2020, in *Society of Photo-Optical Instrumentation Engineers (SPIE) Conference Series*, Vol. 11447, Society of Photo-Optical Instrumentation Engineers (SPIE) Conference Series, 114475K
- Pál, A. 2008, *MNRAS*, 390, 281
- Parviainen, H., Palle, E., Zapatero-Osorio, M. R., et al. 2020, *A&A*, 633, A28
- Parviainen, H., Palle, E., Zapatero-Osorio, M. R., et al. 2021, *A&A*, 645, A16
- Parviainen, H., Tingley, B., Deeg, H. J., et al. 2019, *A&A*, 630, A89
- Petrovich, C., Deibert, E., & Wu, Y. 2019, *AJ*, 157, 180
- Petrovich, C., Muñoz, D. J., Kratter, K. M., & Malhotra, R. 2020, *ApJ*, 902, L5
- Rasmussen, C. E. & Williams, C. K. I. 2006, *Gaussian Processes for Machine Learning*

- Roberts, S., Osborne, M., Ebdon, M., et al. 2012, *Philosophical Transactions of the Royal Society of London Series A*, 371, 20110550
- Sahu, K. C., Casertano, S., Bond, H. E., et al. 2006, *Nature*, 443, 534
- Sanchis-Ojeda, R., Rappaport, S., Pallè, E., et al. 2015, *ApJ*, 812, 112
- Sanchis-Ojeda, R., Rappaport, S., Winn, J. N., et al. 2014, *ApJ*, 787, 47
- Short, D. R., Welsh, W. F., Orosz, J. A., Windmiller, G., & Maxted, P. F. L. 2019, *Research Notes of the American Astronomical Society*, 3, 117
- Silverstein, M. L., Schlieder, J. E., Barclay, T., et al. 2021, arXiv e-prints, arXiv:2110.12079
- Skrutskie, M. F., Cutri, R. M., Stiening, R., et al. 2006, *AJ*, 131, 1163
- Smith, J. C., Stumpe, M. C., Van Cleve, J. E., et al. 2012, *PASP*, 124, 1000
- Stassun, K. G., Oelkers, R. J., Paegert, M., et al. 2019, *The Astronomical Journal*, 158, 138
- Stumpe, M. C., Smith, J. C., Catanzarite, J. H., et al. 2014, *PASP*, 126, 100
- Tamura, M., Suto, H., Nishikawa, J., et al. 2012, in *Society of Photo-Optical Instrumentation Engineers (SPIE) Conference Series*, Vol. 8446, *Ground-based and Airborne Instrumentation for Astronomy IV*, ed. I. S. McLean, S. K. Ramsay, & H. Takami, 84461T
- Tsiaras, A., Waldmann, I. P., Rocchetto, M., et al. 2016, *ApJ*, 832, 202
- Uzsoy, A. S. M., Rogers, L. A., & Price, E. M. 2021, *ApJ*, 919, 26
- Valsecchi, F., Rasio, F. A., & Steffen, J. H. 2014, *ApJ*, 793, L3
- Wang, J., Fischer, D. A., Horch, E. P., & Huang, X. 2015, *ApJ*, 799, 229
- Winn, J. N., Sanchis-Ojeda, R., & Rappaport, S. 2018, *New A Rev.*, 83, 37
- Winn, J. N., Sanchis-Ojeda, R., Rogers, L., et al. 2017, *AJ*, 154, 60
- Zhu, W. & Dong, S. 2021, arXiv e-prints, arXiv:2103.02127
- 
- <sup>1</sup> Instituto de Astrofísica de Canarias (IAC), 38205 La Laguna, Tenerife, Spain
- <sup>2</sup> Departamento de Astrofísica, Universidad de La Laguna (ULL), 38206, La Laguna, Tenerife, Spain
- <sup>3</sup> INAF- Palermo Astronomical Observatory, Piazza del Parlamento, 1, 90134 Palermo, Italy
- <sup>4</sup> University of Palermo, Department of Physics and Chemistry “Emilio Segrè”
- <sup>5</sup> Komaba Institute for Science, The University of Tokyo, 3-8-1 Komaba, Meguro, Tokyo 153-8902, Japan
- <sup>6</sup> Astrobiology Center, 2-21-1 Osawa, Mitaka, Tokyo 181-8588, Japan
- <sup>7</sup> Center for Astrophysics | Harvard & Smithsonian, 60 Garden Street, Cambridge, MA 02138, USA
- <sup>8</sup> The Maury Lewin Astronomical Observatory, Glendora, California, 91741, USA
- <sup>9</sup> Université de Montréal, Département de Physique, IREX, Montréal, QC H3C 3J7, Canada
- <sup>10</sup> Observatoire du Mont-Mégantic, Université de Montréal, Montréal, QC H3C 3J7, Canada
- <sup>11</sup> European Space Agency (ESA), European Space Research and Technology Centre (ESTEC), Keplerlaan 1, 2201 AZ Noordwijk, The Netherlands
- <sup>12</sup> Japan Science and Technology Agency, PRESTO, 3-8-1 Komaba, Meguro, Tokyo 153-8902, Japan
- <sup>13</sup> National Astronomical Observatory of Japan, 2-21-1 Osawa, Mitaka, Tokyo 181-8588, Japan
- <sup>14</sup> Department of Astronomy, Graduate School of Science, The University of Tokyo, 7-3-1 Hongo, Bunkyo-ku, Tokyo 113-0033, Japan
- <sup>15</sup> Okayama Observatory, Kyoto University, 3037-5 Honjo, Kamogatacho, Asakuchi, Okayama 719-0232, Japan
- <sup>16</sup> Department of Multi-Disciplinary Sciences, Graduate School of Arts and Sciences, The University of Tokyo, 3-8-1 Komaba, Meguro, Tokyo 153-8902, Japan
- <sup>17</sup> Department of Astronomical Science, The Graduated University for Advanced Studies, SOKENDAI, 2-21-1, Osawa, Mitaka, Tokyo, 181-8588, Japan
- <sup>18</sup> Swedish National Space Agency Fellow
- <sup>19</sup> Department of Space, Earth and Environment, Astronomy and Plasma Physics, Chalmers University of Technology, 412 96 Gothenburg, Sweden
- <sup>20</sup> Instituto de Astrofísica de Andalucía (IAA-CSIC), Glorieta de la Astronomía s/n, 18008 Granada, Spain
- <sup>21</sup> Institute of Astronomy and Astrophysics, Academia Sinica, P.O. Box 23-141, Taipei 10617, Taiwan, R.O.C.
- <sup>22</sup> Department of Astrophysics, National Taiwan University, Taipei 10617, Taiwan, R.O.C.
- <sup>23</sup> Department of Earth and Planetary Science, Graduate School of Science, The University of Tokyo, 7-3-1 Hongo, Bunkyo-ku, Tokyo 113-0033, Japan
- <sup>24</sup> National Astronomical Observatory of Japan, 2-21-1 Osawa, Mitaka, Tokyo 181-8588, Japan
- <sup>25</sup> Department of Earth and Planetary Sciences, Tokyo Institute of Technology, Meguro-ku, Tokyo, 152-8551, Japan
- <sup>26</sup> Astrobiology Research Unit, Université de Liège, 19C Allée du 6 Août, 4000 Liège, Belgium
- <sup>27</sup> Department of Earth, Atmospheric and Planetary Science, Massachusetts Institute of Technology, 77 Massachusetts Avenue, Cambridge, MA 02139, USA
- <sup>28</sup> Space sciences, Technologies and Astrophysics Research (STAR) Institute, Université de Liège, Belgium
- <sup>29</sup> Oukaimeden Observatory, High Energy Physics and Astrophysics Laboratory, Cadi Ayyad University, Marrakech, Morocco
- <sup>30</sup> George Mason University, 4400 University Drive, Fairfax, VA, 22030 USA
- <sup>31</sup> Department of Physics & Astronomy, Swarthmore College, Swarthmore PA 19081, USA
- <sup>32</sup> Patashnick Voorheesville Observatory, Voorheesville, NY 12186, USA